JOURNAL OF MATERIALS SCIENCE 21 (1986) 3097–3107

A study of the microstructure, mechanical properties and failure behaviour of Al–Li–Co melt-spun ribbons: effect of Al_9Co_2 phase particle precipitation

FAWZY H. SAMUEL*
Laboratoire de Physique du Solide, Ecole des Mines, Parc de Saurupt, 54042 Nancy Cedex, France

The present work is performed on three alloys, namely Al–2.8Li–0.1Co, Al–2.8Li–0.4Co and Al–2.8Li–0.8Co (all wt%) produced by melt-spinning. Their microstructures in the as-melt-spun condition as well as following ageing at 473 K are studied by light and transmission electron microscopy where the phases present have been identified using X-ray diffractometry. The mechanical properties of these alloys are characterized by longitudinal tensile tests as well as by hardness measurements. The results reveal that increasing the cobalt content and hence the volume fraction of Al_9Co_2 dispersoids is very effective in increasing both yield and tensile strengths, in addition to a noticeable improvement in the ductility. Simple empirical equations are proposed to determine the yield strength in the as-melt-spun and aged conditions. The Young's modulus for the first alloy has been calculated from a bending test and is found to lie between 80 and 83 GPa depending on the ageing condition. Another advantage of increasing the Al_9Co_2 concentration appears in promoting high-energy transgranular fracture instead of the low-energy intergranular fracture usually observed in Al–Li alloys subjected to ageing.

1. Introduction

Aluminium–lithium alloys possess the commercially attractive combination of a high specific strength and high specific modulus [1]. However, their application has been slowed down by difficulties relating to the loss of lithium during melting and ingot casting [2]. In order to overcome these problems, a rapid solidification technique has been suggested to produce alloys with a high degree of microstructural refinement that is preserved through the hot consolidation and heat-treatment steps [3]. Strengthening in Al–Li alloys is associated with the precipitation of a high volume fraction of the metastable phase $\delta'(Al_3Li)$ owing to its resistance to dislocation motion [3]. The strengthening effect due to long-range ordering of Al_3Li is reduced when the precipitates are sheared by dislocations. This leads to a successive decrease in resistance of the δ' particles for further dislocations, and consequently results in planar slip and a tendency towards strain localization and distortion of the Al_3Li [3]. The slip distribution in Al–Li alloys depends on the magnitude of local work-softening that occurs during deformation.

It is interesting to note that while there is ample literature available on the ingot, powder and consolidated/compact forms of Al–Li alloys, not much information is to be found on the melt-spun ribbon forms of these alloys. Thus the present study, where the structural characteristics and mechanical behaviour of melt-spun ribbons of Al–Li–Co alloys have been investigated, may well be one of the first of its kind in this field.

The purpose of this work is to determine the role of rapid solidification and precipitation of fine incoherent dispersoid particles of Al_9Co_2 phase resulting from minor additions of cobalt (between 0.1 and 0.8 wt%) for promoting homogenized slip and improving the alloy ductility of melt-spun ribbons without prior consolidation. These effects are correlated with changes in the elastic modulus, tensile properties and fracture modes in this system. For comparison, data on Al–3 wt% Li–0.1 wt% Co ingot-processed alloy have been obtained following solution heat-treatment at 811 K for 0.5 h.

2. Experimental technique

The experiments were performed on three Al–Li–Co alloys produced by melt-spinning (MS). For alloy chemistry, see Table I. The alloys were prepared from high-purity aluminium, lithium and cobalt metals under an inert atmosphere of helium. The alloys were spun into ribbons by conventional melt-spinning using a copper disc as the rotating chilled substrate. The melt-spinning was done in a chamber under helium atmosphere. The ribbon width was typically 1500 μm with a thickness lying in the range 30 to 40 μm. All the ribbons were aged at 473 K for various times up to 100 h without prior solution heat-treatment.

---

*On leave of absence from the Central Metallurgical Research and Development Insitute, National Research Centre, Dokki, Cairo, Egypt.

0022-2461/86 $03.00 + .12

TABLE I Alloy chemistry

Code	Fabrication technique	Designation	Form	Alloy composition (wt %)
10ALCR	Melt spinning	MS	Ribbon	Al–2.85 Li–0.1 Co
40ALCR	Melt spinning	MS	Ribbon	Al–2.85 Li–0.4 Co
80ALCR	Melt spinning	MS	Ribbon	Al–2.85 Li–0.8 Co
10ALCI	Ingot metallurgy	IM	10 mm round ingot	Al–3 Li–0.1 Co

For the 80ALCR ribbons, ageing was also carried out after solution heat-treatment at 811 K for 0.5 h (MS + SHT).

Detailed metallographic examinations were made on the alloys in different conditions, employing standard light and transmission electron microscopy (TEM). The foils were investigated in a JEOL 200CX electron microscope operating at 200 kV and various specimen inclinations were adopted. Modulus measurements were carried out on the 10ALCR ribbons, after careful polishing, using a bending test technique developed in our laboratory and shown schematically in Fig. 1. Values reported are the average of at least five readings. The yield strength (0.2% offset), ultimate tensile strength and the elongation were measured from longitudinal tensile test ribbons (20 mm gauge length and 1.5 mm width) using a strain rate of $6 \times 10^{-4}\,\mathrm{sec}^{-1}$. All tests were conducted at room temperature and the averages of at least five readings are reported here. Fracture surfaces were studied by a scanning electron microscope operating at 25 kV. X-ray diffraction patterns were obtained from both wheel and gas surfaces using a Co$K\alpha$ source for each working condition. However, the results showed no significant difference between the two mentioned surfaces.

3. Results and discussion

3.1. Microstructure

3.1.1. Initial structure

Garett and Sanders [4] have reported that melt-spinning of hypereutectic Al–Co alloys leads to the formation of two zones possessing different microstructural characteristics. Zone A (wheel side) is characterized by fine primary aluminium dendrites and appears to be featureless through the light microscope, whereas Zone B (gas side), is characterized by coarse Al_9Co_2 particles surrounding the primary aluminium dendrites and showing a good response to etching. Fig. 2 represents the microstructures from through-thickness cross-sections of two alloys that are hypo-eutectic (with respect to the Al–Co binary diagram). As can be seen in all cases, the solidification started by columnar formation that extended throughout the entire thickness. These columns are not always perpendicular to the ribbon direction and they are often found making an angle of 75 to 80°. In addition, we found that these alloys offered good resistance to etching as is clearly visible from Fig. 2.

TEM has yielded valuable information on the structural refinement resulting from the high freezing rate associated with the melt-spinning process. This is evident in the very fine grains (1 to 3 μm) as displayed in Fig. 3a (a cross-section normal to a set of columnar grains, nearly at the middle of the ribbon). Scattered particles of Al_9Co_2 phase are seen inside the grains. The dispersoid parameters deduced from TEM micrographs of the present alloys are listed in Table II. At triple meeting points of high-angle grain boundaries, fairly coarse Al_9Co_2 particles are frequently observed as shown in Fig. 3b. Increasing the cobalt content up to 0.4 wt % resulted in a noticeable increase in the number of Al_9Co_2 phase particles, as shown in Fig. 4a. In some places, coarser microprecipitates are stretched parallel to the grain-boundary dislocation lines as inferred from Fig. 4b, which is a dark-field image showing Al_9Co_2 precipitates parallel to one preferential direction. For the highest cobalt content, 0.8 wt %, which is very close to the eutectic composition 1 wt %, precipitation of Al_9Co_2 is found to occur at grain boundaries as well as in the matrix. The work of Unwin and Nicholson [5] shows that the

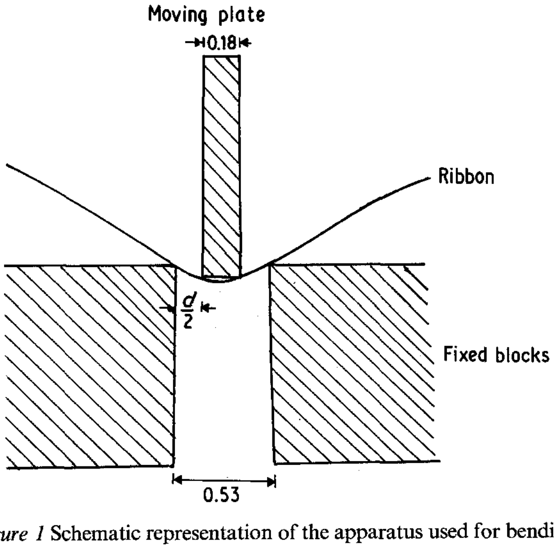

Figure 1 Schematic representation of the apparatus used for bending test. All dimensions are in mm.

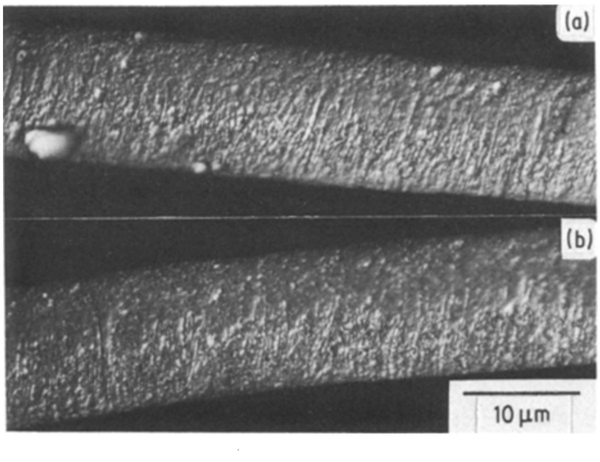

Figure 2 Light optical micrographs of Al–Li–Co ribbons in the as-melt-spun condition: (a) 10ALCR, (b) 80ALCR.

TABLE II Dispersoid parameters in Al–Li–Co alloys (present work)

Alloy	D (nm)*	L (nm)†
10ALCR	38	375
40ALCR	60	290
80ALCR	100	135

*D = mean particle diameter.
†L = mean planar centre-to-centre Al_9Co_2 dispersoid spacing.

precipitate nucleation rate and precipitate morphology at grain boundaries in aluminium-based alloys are determined by grain-boundary plane misorientation, crystallographic matching between the precipitate habit plane and the grain-boundary plane, and grain-boundary inclination. Unwin and Nicholson have attributed variations in precipitate density and morphology to the deviation from boundary coincidence and to the effect of the changes in the grain-boundary plane. For a given quench rate, the density of precipitates at random grain boundaries increases with an increase in the quenching temperature, due to the effect of solute segregation during quench. Fig. 5a reveals dense precipitation of Al_9Co_2 on a slightly curved high-angle grain boundary. We have also noted a change in the precipitate direction with change in the grain-boundary orientation (follow the arrows). Also, the precipitate particle size at the grain boundary is larger than in the matrix because solute segregation and the enhanced solute diffusivity along grain boundaries both increase the rate at which solute atoms join any critical nucleus. Another feature of grain-boundary precipitation is shown in Fig. 5b, where relatively thick plates of Al_9Co_2 are viewed. However, these plates are not always flat, a noticeable branching being often observed (Figs 5c and d).This may be due to the fact that we are dealing with a eutectic alloy, and branching will then occur to maintain the interlamellar or particle spacing at the growth front. In most of the cases, the grain boundary was of high angle with slight curvature. The change in the precipitate morphology may be caused by the variation in the grain-boundary plane orientation from that favouring one variant of the precipitate to that favouring another.

On the other hand, broad ledges, a common structural feature of high-angle grain boundaries, act as preferential sites for precipitate nucleation which results in a non-uniform precipitate distribution along the length of a grain boundary [6]. Lartique and Priester [7] have further found that stabilized extrinsic grain-boundary dislocations may act as concentration sites for segregated species and lead to precipitation, either (i) discontinuous precipitation on a dislocation line, by a preferential diffusion of solute along the dislocation, or (ii) continuous precipitation by a preferential diffusion of atoms along the boundary towards the dislocation. Since we expect that the type of precipitation viewed in Fig. 5 will contribute to material brittleness, the specimens were subjected to a simple solution treatment (ST) at 811 K for 0.5 h followed by a cold water quench (CWQ) which was found sufficient to eliminate most of the grain-boundary precipitation and promote matrix precipitation, as displayed in Fig. 6. A similar effect was noticed on prolonged ageing at 473 K, i.e. 16 and 100 h, directly after ribbon formation.

The light microscopy and TEM observations were confirmed by X-ray diffraction, where extra lines from Al_9Co_2 intermetallic precipitates could be detected. Furthermore, the lattice parameters plotted in Fig. 7 decrease linearly with cobalt content for as-melt-spun ribbons. It is evident from this figure that the effect of cobalt is much stronger, giving $(1/a)(\partial a/\partial c) = 0.082\%$, than that of lithium where $(1/a)(\partial a/\partial c) = 0.023\%$. These results emphasize the fact that the amount of cobalt in solid solution in aluminium increases with increasing cobalt content; this results from the increased solid solubility due to rapid solidification (see, for example, Fig. 11 below).

3.1.2. Effect of ageing

Fig. 8a (10ALCR) indicates the breakdown of the solid solution during melt-quenching, resulting in homogeneous dispersion of fine Al_3Li (δ') having a size of approximately 5 nm. According to Grant [8], increasing quench rates promote decreasing grain size. With reference to his results, the cooling rate used in the present study is estimated at about $10^5\,K\,sec^{-1}$. There is some ambiguity concerning the possibility of the formation of the δ' phase on quenching. Noble and Thompson [9] have reported δ' in the solid-stage quenching conditions while others [10, 11] have only observed superlattice reflections from δ' particles of 4 nm diameter. The work of Sanders *et al.* [12] is in

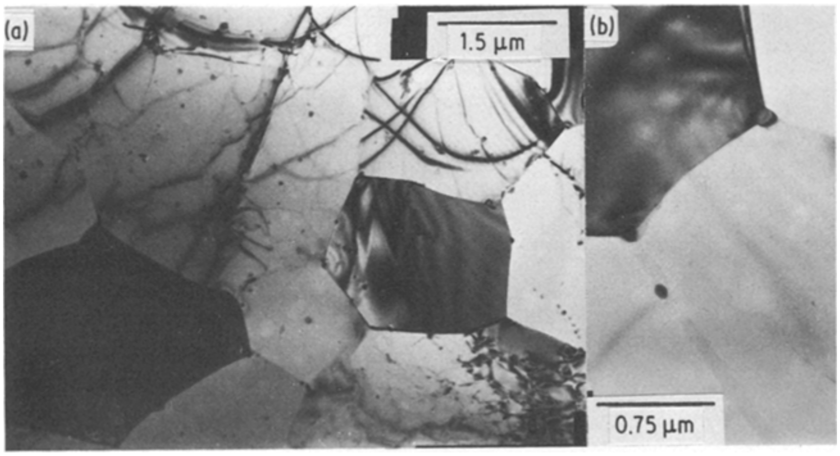

Figure 3 Bright-field micrographs of 10ALCR ribbon in the as-melt-spun condition showing (a) the grain size in a section normal to a set of columnar grains, (b) location of Al_9Co_2 particles at triple meeting points.

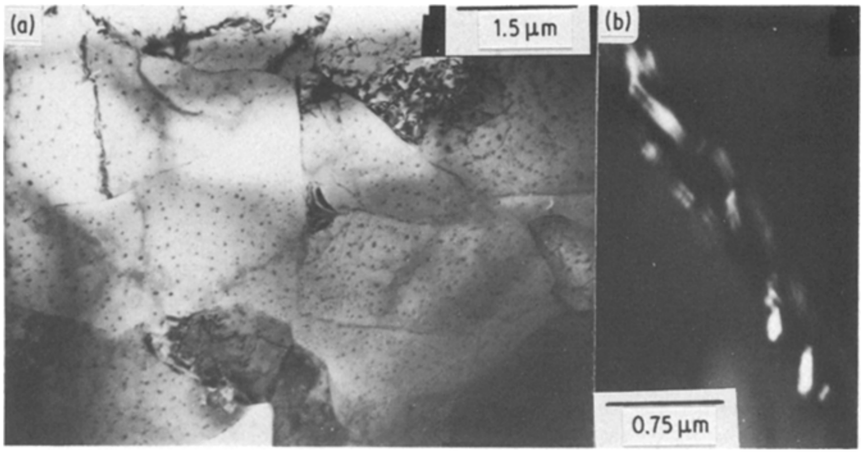

Figure 4 TEM micrographs of 40ALCR ribbon in the as-melt-spun condition showing (a) distribution of Al_9Co_2 dispersoids within the matrix (bright field), (b) preferential precipitation of Al_9Co_2 microprecipitates at the grain boundary (dark field).

conformity with the latter proposal, possibly due to difficulty in suppressing the homogeneous nucleation reaction of the δ' phase even within a very short time (~ 10 min) after quenching and ageing at room temperature. They have attributed this to the small lattice misfit (-0.18%) between the δ' and the fcc matrix as well as to an excess vacancy concentration that is generated on quenching [13].

Representative electron micrographs for δ' precipitation on subsequent ageing of 10ALCR ribbons at 473 K are shown in Figs 8b and c. Well-defined δ' precipitates are observed for ageing times from 1 h up to 100 h. A widening of the precipitate-free zones (PFZs) accompanying time is present. On the basis of the TEM micrographs in Fig. 8, it is found that a spherical shape is the common morphology observed for δ'. After ageing at 473 K for 100 h collinear rows of δ' are observed, sometimes elongated along the line direction (Fig. 8b). In these cases a dislocation is found to be associated with the rows, lying on the common line between particles and on the surfaces of the particles themselves. This may be explained by pipe diffusion. The average coarsening rate at this temperature is about $2.9 \times 10^{-25}\,m^3\,h^{-1}$.

In order to arrive at a better understanding of the growth kinetics of the δ' phase on isothermal ageing, Sanders *et al.* [12] have proposed a model assuming that the growth process is a diffusion-controlled one. This model has the form

$$R - r_0 = Ct^{1/3} \tag{1}$$

where r_0 is the initial δ' particle radius. The best fit to the variation in radius (R) with time ($t^{1/3}$) is illustrated in Fig. 9. As can be seen, the results on ribbons (MS) at 473 K are somewhat lower as compared to those obtained from ingots (IM). With the help of the micrographs in Fig. 8, the observation of the PFZs at 473 K can be discussed on the basis of the vacancy concentration model [14]. According to this model, for the present MS alloys, PFZs will chiefly occur due to loss of vacancies at grain boundaries and homogeneous nucleation is likely to occur with excess vacancies. As a consequence of this process, the PFZs may have widths up to 1 μm which is approximately what we have obtained on holding the specimens at 473 K for 100 h ($\sim 0.7\,\mu$m). To satisfy this condition, one may consider the concentration of vacancies with respect to quenching temperature and rate as well as the PFZ

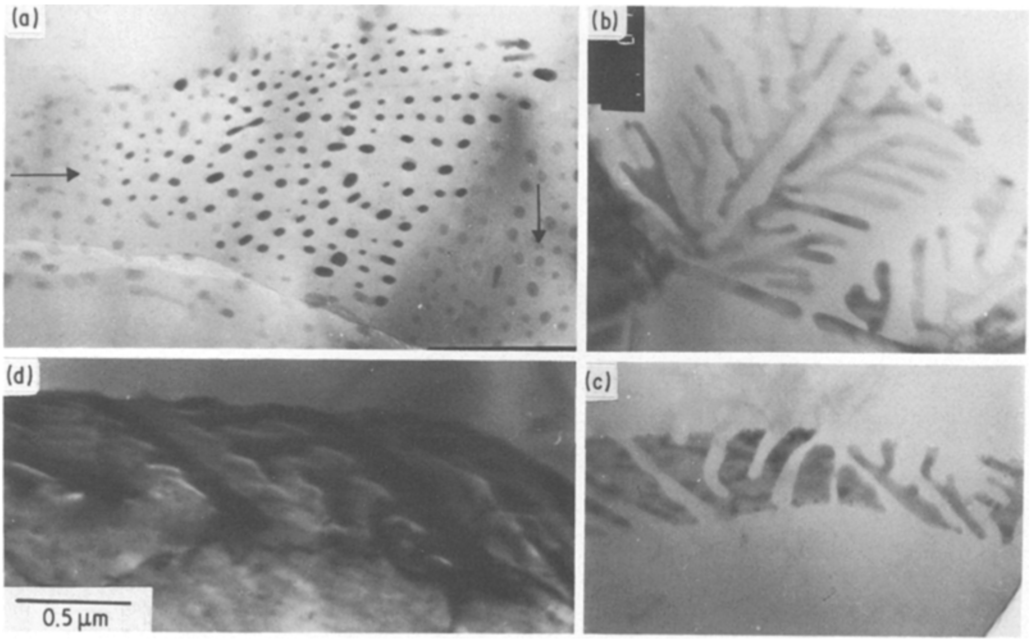

Figure 5 A series of TEM micrographs of 80ALCR ribbon in the as-melt-spun condition showing different morphologies of Al_9Co_2 precipitates at grain boundaries. Note the curvature of the grain boundary in each case.

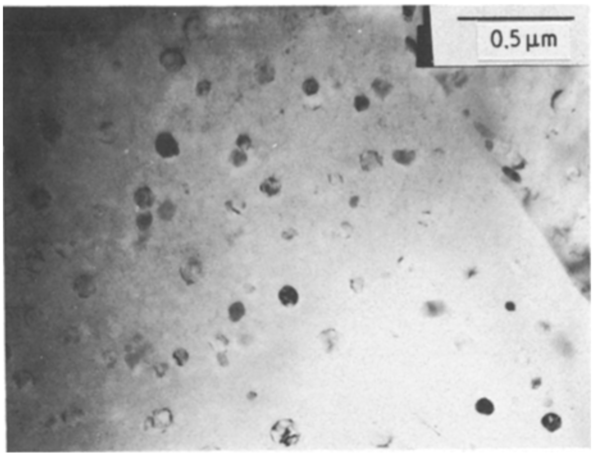

Figure 6 Bright-field micrograph of 80ALCR ribbon following solution heat-treatment at 811 K for 0.5 h.

volume fraction with respect to grain size, δ' volume fraction and lithium in solid solution. Given the fact that coarse particles due to δ' or δ are not seen* at the grain boundaries in Fig. 8, we are unable to confirm or repudiate their essentiality for the formation of PFZs.

The growth of PFZs was analysed in the light of the following equation [12],

$$W/2 = Ct^{1/3} \tag{2}$$

where W is the width of the PFZ in micrometres and t is the time in seconds. The data are plotted in Fig. 10. Although the values reported here are in good accordance with those measured by Sanders *et al.* [12] on Al–2.7 wt % Li–0.2 wt % Mn alloy and the IM alloy (grain sizes in the range of 100 to 150 μm and 80 to 100 μm, respectively), the MS alloy shows a remarkably higher PFZ volume fraction.

A series of micrographs emphasizing the role of rapid solidification in increasing the extent of solid solubility of cobalt are shown in Figs 11a to d for 40ALCR and 80ALCR ribbons. It is inferred from these micrographs that an important fraction of cobalt, more than 0.2% [15], was in solid solution after melt-quenching and that it decomposed uniformly

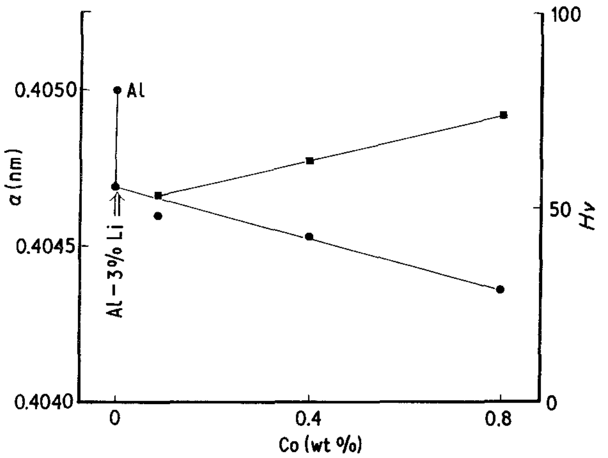

Figure 7 (●) Lattice parameters and (■) Vickers microhardness values.

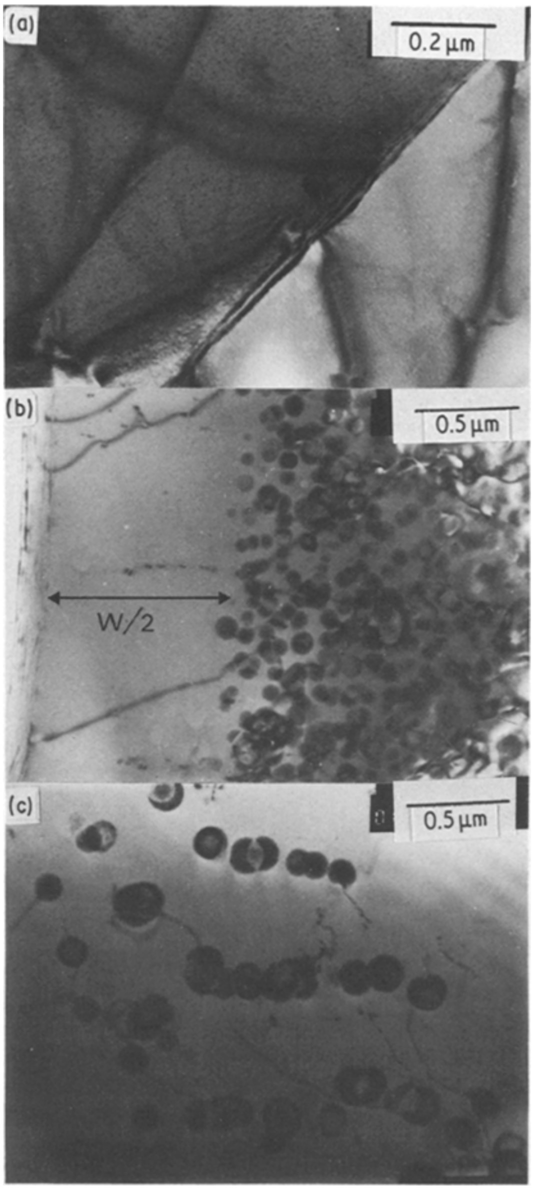

Figure 8 Bright-field micrographs of 10ALCR ribbon following ageing at 473 K for different ageing times: (a) 0 h, (b) 100 h, (c) 120 h.

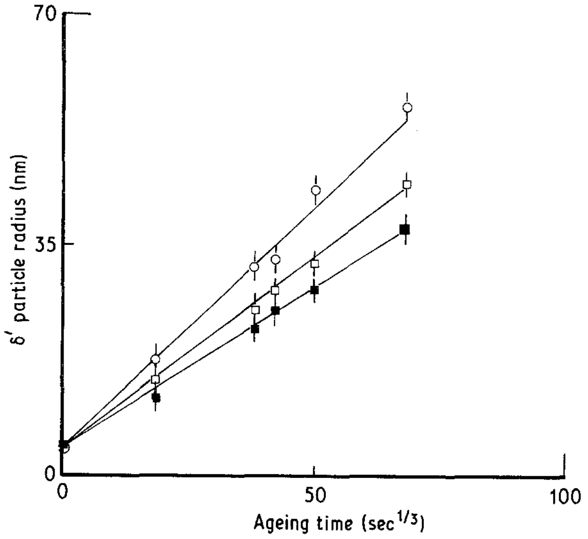

Figure 9 The average δ' precipitate radius as a function of the cube root of ageing time at 473 K: (○) ingot metallurgy alloy (10ALCI), (□) melt-spun ribbon (10ALCR), (■) solution heat-treated melt-spun ribbon (80ALCR).

---

*The equilibrium phase δ(AlLi), which has a cubic structure, occurs on ageing at high temperatures (> 310° C [9–11]) and is incoherent with the aluminium matrix.

TABLE III Modulus and volume fraction of δ' in 10ALCR and 10ALCI alloys

Condition	δ' (vol %)	$E_{\text{calc.}}$ (GPa)	$E_{\text{meas.}}$ (GPa)	Specific modulus, E/ϱ (10^6 m)
10ALCR alloy				
MS	14	81.65	79.70	3.237
MS + 1 h at 473 K	22	82.37	81.90	3.329
MS + 16 h at 473 K	28	83.41	82.50	3.321
10ALCI alloy				
IM	12	80.65	80.32	3.346
IM + 1 h at 473 K	18	81.65	80.45	3.258
IM + 24 h at 473 K	24	82.70	81.20	3.288

throughout the grains after ageing. This observation is expected to contribute to strengthening of the soft PFZs noticed in 10ALCR (for comparison see Fig. 8b).

3.2. Mechanical properties

3.2.1. Young's modulus measurements

The results of the Young's modulus determination for both 10ALCR and 10ALCI alloys are shown in Table III. The data from bending tests have been analysed using a model of the form

$$F\frac{d}{2} = E\frac{le^3}{1-\nu^2}\frac{1}{12}\frac{1}{R} \qquad (3)$$

where F is the applied force, $d/2$ is the distance shown in Fig. 1, l and e are the ribbon width and thickness, respectively, ν is Poisson's ratio, R is the curve radius and E is Young's modulus. In both alloys, the value of the modulus increases with increasing δ' volume fraction, from a value of 80 GPa at 12 vol % of δ' to 83 GPa at 28 vol % of δ'. According to the present bending technique the maximum deviation from that reported by Noble *et al.* [16] is less than 5%. Since the values are found to be nearly the same for both alloys with respect to the ageing condition, this indicates that the major contribution to the modulus, in addition to lithium in solid solution (~62%), comes from the high volume fraction of Al_3Li (~38%) and the role of the grain size or the δ' particle size is of no particular importance. The findings of Noble *et al.* [16] on Al–3 wt % Li alloy exhibit that the modulus increases from 66 GPa to 78.5 GPa due to lithium in solid solution, and from 78.5 to 83 GPa due to $\delta'(Al_3Li)$ precipitation on ageing at 473 K. The work of Sanders and Starke [3] on Al–2.3 wt % Li indicates that the δ' phase is not necessary to increase the elastic modulus. This conclusion is in conformity with the results of Gysler *et al.* [17] and Harris [18] and is more related to the presence of short-range order in their alloys.

To investigate the influence of δ' volume fraction on the value of E, the Rule of Mixture equation

$$E_{\text{aged}} = E_{\text{m}}V_{\text{m}} + E_{\delta'}V_{\delta'} \qquad (4)$$

was utilized assuming E_{m} at 1.6 wt % Li ≅ 78.5 GPa and $E_{\delta'} = 96$ GPa [16]. The results are listed in Table III. As can be noticed, the maximum difference between the calculated values and those produced experimentally is about 3%. One important advantage of increasing the elastic modulus of aluminium alloys by lithium addition as well as precipitation of δ' is the simultaneous increase in the specific modulus. Using a density (ϱ) of 2469 kg m^{-3} as determined experimentally, the values of E/ϱ were estimated. These are reported in Table III.

3.2.2. Tensile properties and dislocation structure

Typical stress–strain curves obtained from a series of tensile tests performed on 10ALCR ribbons in the as-melt-spun condition, as well as following ageing at 473 K for ageing times ranging between 1 and 100 h, are represented in Fig. 12. The yield stress (0.2% YS)

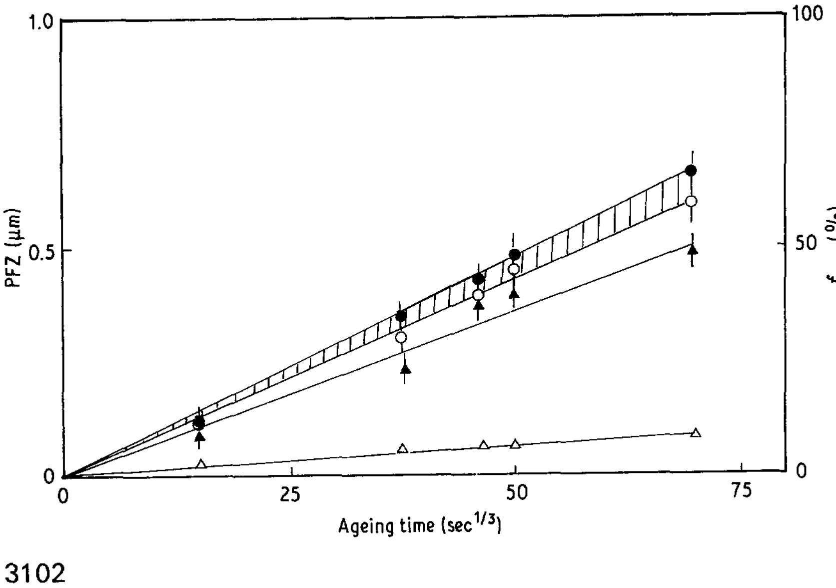

Figure 10 (○, ●) PFZ half-width and (△, ▲) volume fraction of PFZ as a function of the cube root of the ageing time at 473 K. (○, ▲) melt-spun ribbon (10ALCR); (●) solution heat-treated melt-spun ribbon (80ALCR); (△) ingot metallurgy ribbon (10ALCI).

TABLE IV Room temperature tensile properties

Alloy	Treatment	YS (MPa)	UTS (MPa)	El (%)*	YS/ϱ (m)	UTS/ϱ (m)
10ALCR	MS	70	197	15	28.35	79.80
	MS + 16 h at 473 K	290	385	3.5	117.45	155.93
	MS + 100 h at 473 K	180	308	7	72.90	124.74
40ALCR	MS	94	221	18	30.70	89.51
	MS + 16 h at 473 K	324	400	5	131.22	162.00
	MS + 100 h at 473 K	189	336	9	76.55	136.10
80ALCR	MS	119	246	20	48.19	99.64
	MS + 16 h at 473 K	349	440	6	141.30	178.20
	MS + 100 h at 473 K	205	348	10	83.00	141.00

*El (%) is the total elongation in per cent.

and ultimate tensile stress (UTS) for a variety of Al–Li–Co ribbons in either as-melt-spun condition or after ageing are listed in Table IV. The YS and UTS of as-melt-spun ribbons in under-, peak- and over-aged conditions are increasing with the increase in cobalt content. The increased strength levels are mainly due to Al_9Co_2 volume fraction in the as-melt-spun condition which persisted during ageing at 473 K. The strength of aged Al–Li alloys depends to a great extent on the volume fraction of the strengthening particles (δ' Al_3Li), which is determined by the amount of lithium solute available for precipitation [19]. It should be noted, also, that rapid solidification enhances the strengthening for shorter times (~16 h for 10ALCR) as compared to the ordinary casting technique (~24 h for 10ALCI). This is partly attributed to the larger volume fraction of PFZs in the MS ribbon (~25 to 30%) than in the IM counterpart alloy (~3 to 5%).

The relationship between total elongation and cobalt content for MS ribbons is also shown in Table IV. The overall improvement in ductility on increasing the cobalt content, and in turn the volume fraction of Al_9Co_2, arises from the dispersal of the slip by the dispersoid particles. Besides the presence of Al_9Co_2, the coarsening of δ' also improves ductility. The substructures of the ribbons deformed in tension are shown in Figs 13 and 15 (below). The deformation substructure of Al–Li–0.1 wt % Co aged at 473 K for 16 h (peak-aged condition) reveals intense planar slip with the dislocations arrayed in parallel bands (Fig. 13a). It is evident from the corresponding dark field (Fig. 13b, using a δ' diffracted beam) that the precipitates within the bands are severely sheared as

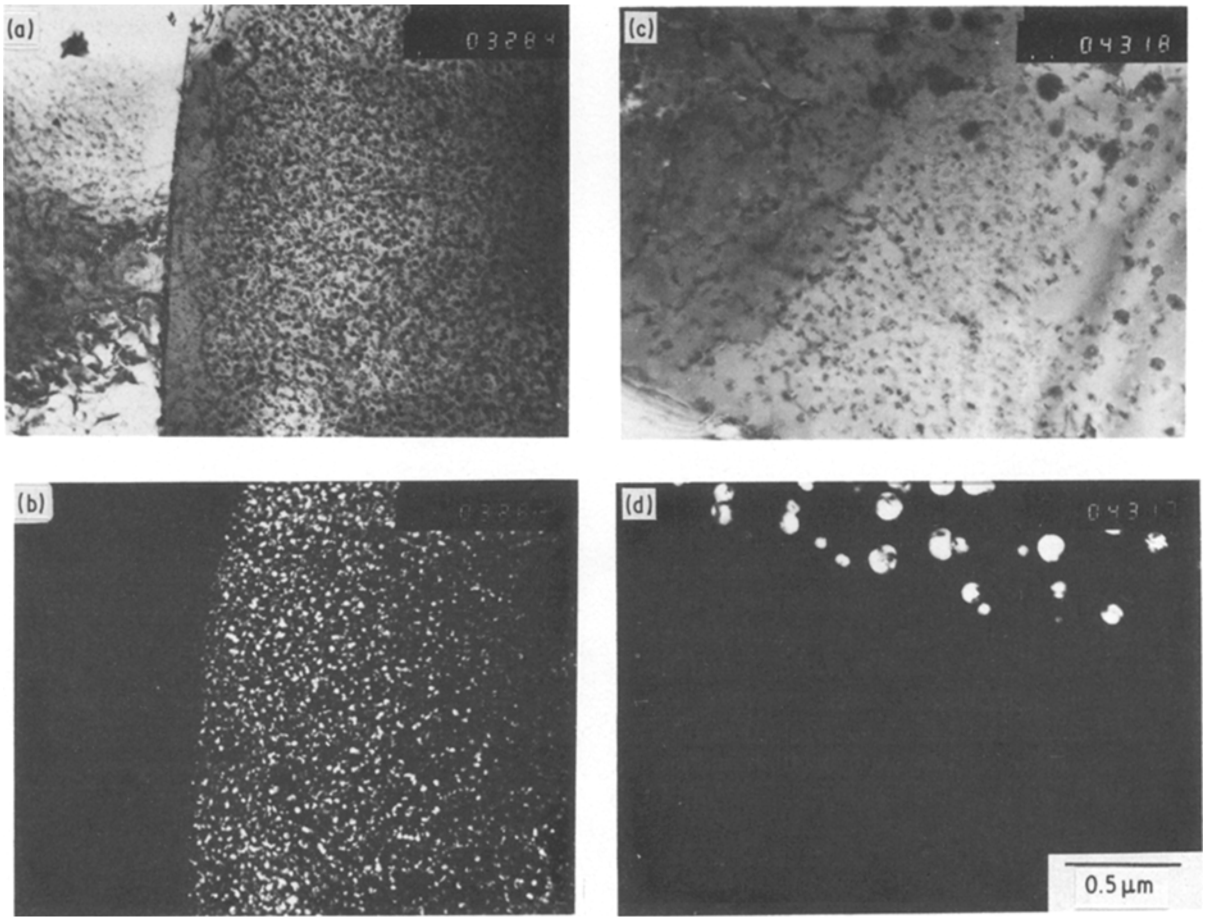

Figure 11 TEM micrograph of melt-spun ribbons following ageing at 473 K: (a) 40ALCR, 16 h, bright field; (b) 40ALCR, 16 h, dark field imaged on a δ' reflection; (c) 80ALCR, 100 h, bright field; (d) 80ALCR, 100 h, dark field imaged on a δ' reflection.

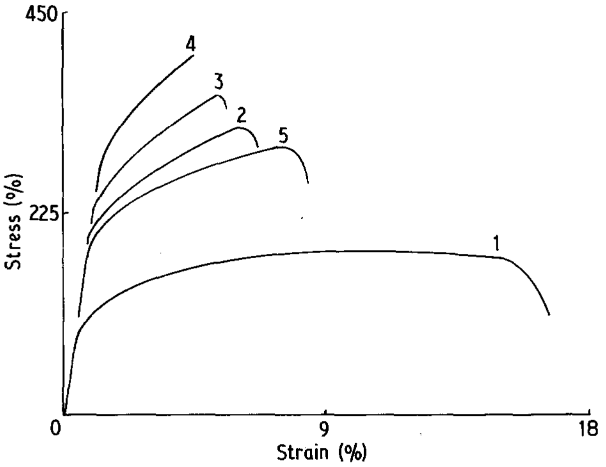

Figure 12 Stress–strain curves obtained from 10ALCR ribbons following ageing at 473 K for (1) 0 h, under-aged; (2) 1 h; (3) 8 h; (4) 16 h, peak-aged; (5) 100 h, over-aged condition.

compared to those in the matrix. In addition, these bands are causing mutual offsets in the grain boundary (see Fig. 18 below).

The increase of critical resolved shear stress (CRSS, τ) owing to the force of interaction between flexible dislocation pairs and ordered misfit-free particles is chiefly governed by the following relation [20],

$$\tau \propto f_0^{1/2} r_0^{1/2} \tag{5}$$

where f_0 and r_0 are the δ' particle volume fraction and mean particle radius, respectively. The findings of Sanders and Starke [3] show that the magnitude of $f_0^{1/2} r^{1/2}$ will be proportional to the degree of localized work-softening on the glide planes, where the ordered δ' particles are sheared by the dislocations. The yield stresses of 10ALCR and 10ALCI are plotted as a function of the product $f_0^{1/2} r_0^{1/2}$ for δ' in Fig. 14. The findings of Sanders and Starke [3] on Al–(1.6 to 2.3) wt % Li are superimposed for comparison. It is interesting to note that when the composition of the alloys exceeds the $\alpha/(\alpha + \delta')$ boundary (at 1.6 wt % Li, where lithium can be present as δ'), it is possible that they may have different $f_0^{1/2} r_0^{1/2}$ values depending on ageing time and temperature. Thus, the importance of the production method and lithium concentration is to decide the YS level. Based on the foregoing discussion, it would be expected that the Al–Li–0.1 wt % Co MS and IM alloys will exhibit a tendency for planarity and inhomogeneity of slip which depends on the degree of ageing.

Fig. 15 shows a TEM micrograph (bright field) of the 10ALCR ribbon in the over-aged condition (100 h at 473 K) deformed till fracture. In this case δ' particles are non-shearable as seen in Fig. 15b (using a δ' diffracted beam). The average distance between the precipitates is found to be ~0.1 μm for a particle radius, r_0, about 0.05 μm (see also Fig. 9). Orowon hardening is thus suggested to be the predominant hardening mechanism. Following Ashby's argument [21], the stress–strain equation can be written as

$$\sigma \sim \mu \boldsymbol{b}(\varrho^{\mathrm{G}} + \varrho^{\mathrm{s}})^{1/2} \tag{6}$$

where μ is the shear modulus, $\boldsymbol{b}$ the Burgers vector, ϱ^{G} the density of the geometrically-necessary dislocations and ϱ^{s} the density of statistically-stored dislocations with tensile strain. The value of ϱ^{G} can be expressed as

$$\varrho^{\mathrm{G}} \sim \frac{1}{\lambda^{\mathrm{G}}} \frac{4\gamma}{\boldsymbol{b}} \tag{7}$$

where γ is the shear strain. For alloys containing more or less spherical particles, $\lambda^{\mathrm{G}} = r_0/f_0$ (about 10^{-2} μm from Fig. 15b). If $\varrho^{\mathrm{G}} \gg \varrho^{\mathrm{s}}$, then ϱ^{G} controls the stress–strain curve.

The relationship between work-hardening rate (WHR) and ultimate tensile strength is demonstrated in Fig. 16 for 10ALCR, based on at least five tensile

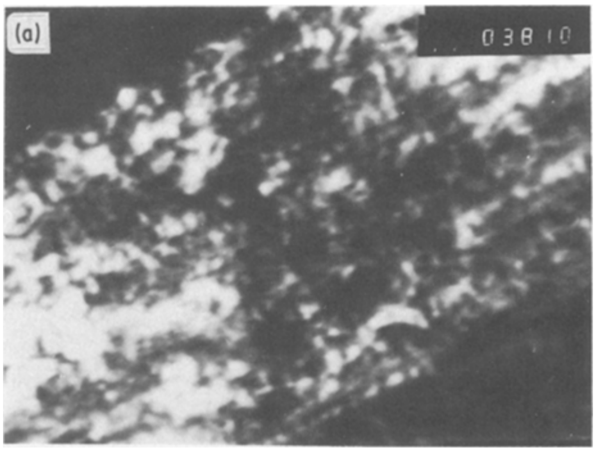

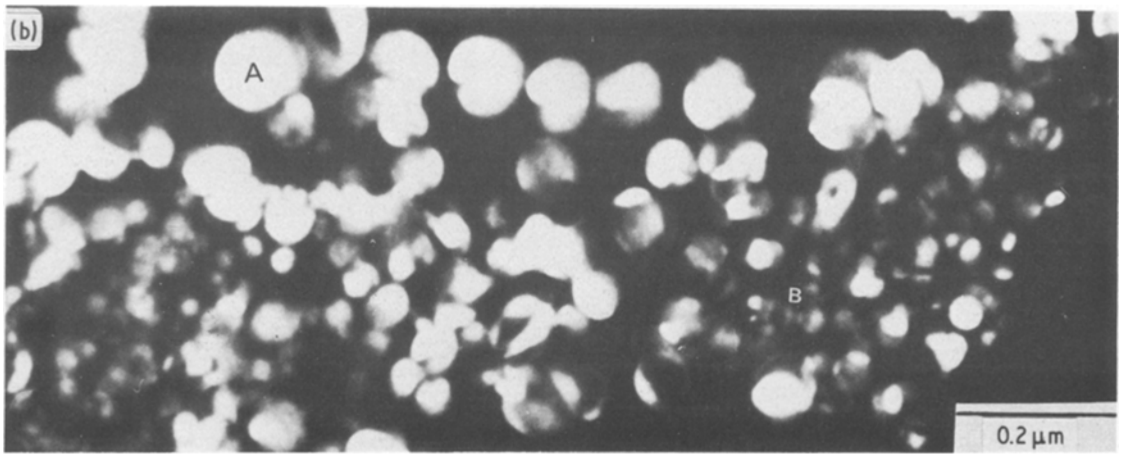

Figure 13 TEM micrographs of 10ALCR ribbons aged at 473 K for 16 h and pulled to failure: (a) a slip band, bright field; (b) distortion of δ' particles within the slip band (B) as compared to those at the boundary of the slip band (A) (dark field imaged on a δ' reflection).

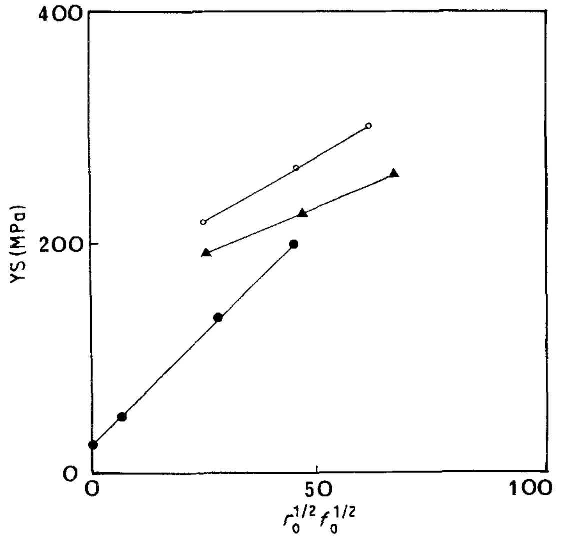

Figure 14 YS plotted as a function of the product of the size and volume fraction of δ' for (○) 10ALCR ribbons and (▲) 10ALCI ingots following ageing at 473 K for times ranging between 1 h and 16 h. (●) Data from Sanders and Starke [3].

tests for each given condition. Deformation beyond yield stress in both MS and IM alloys leads to a substantial increase in the work-hardening rate, suggesting a considerable increase in dislocation density. Since the process is stimulated by precipitate formation on ageing, this will tend to impede the motion of dislocations and hence reduce their velocity. This observation leads us to propose a development of strain localization during deformation at under- and peak-aged conditions for shearable δ' (Al_3Li) phase particles, and less or no localization for non-shearable δ' particles depending on their radius and interparticle distance which, in turn, represents the mean slip distance.

Tamler and Kanert [22] have described the work-hardening rate on the basis of the internal stress, τ_i, and mean jump distance, L, as follows:

$$\mathrm{WHR} = \frac{A}{\tau_i \dfrac{\mathrm{d}L}{\mathrm{d}\tau_i} + L} \qquad (8)$$

where A is a constant. As $\mathrm{d}L/\mathrm{d}\tau_i$ is a negative term, it leads to a conclusion that the work-hardening rate of Al–Li containing non-shearable precipitates is expected to be higher than in Al–Li containing shearable precipitates. Recalling Fig. 12 in combination with Fig. 16 reveals that this relation holds true for as-MS and MS ribbons aged at 473 K for 100 h (see Figs 8 and 15) only, whereas the reverse is true for Al–Li alloys containing shearable δ' along with soft PFZs for the reasons mentioned in the above paragraph.

The effectiveness of Al_9Co_2 particles as incoherent dispersoids in promoting homogeneous deformation without planar slip is shown in Fig. 17. The ability of the dispersoid particles to disperse slip, coupled with an almost complete absence of coarse, heterogeneous grain-boundary precipitates, is conducive to improved ductility in Al–Li alloys containing cobalt as is evidenced from Table IV. Sankaran *et al.* [23] have discussed the sources of strengthening in Al–Li–Co alloys. The yield strength of as-melt-quenched ribbons is attributed to the contributions from a large number of weak obstacles (solute atoms) and a small number of strong obstacles (dispersoids). The flow stress of MS ribbons in the aged conditions is a superposition of the flow-stress contribution from the Al–Li solid-solution matrix, the δ' precipitates and the dispersoids. Based on the present findings illustrated in Table IV, the best fit between the YS and the alloy composition in the as-melt-spun condition (0.1 and 0.4 wt % Co) or in solution heat-treated condition (0.8 wt % Co) prior ageing at 473 K can be expressed as

$$\begin{aligned} \mathrm{YS(MPa)} &= 22.15(\text{atomic fraction Li})^{1/2} \\ &\quad + 125(\text{atomic fraction Co}) \qquad (9) \end{aligned}$$

After ageing, the estimated strengthening from δ' precipitation is about 220 MPa and the estimated yield strength of Al–1.6 wt % Li is about 43 MPa [3]. The dispersion strengthening contribution was calculated from the modified Orowon relation [21] as well as from Table IV. The former shows 76 MPa as an average value between 61 MPa (for edge dislocation) and 91 MPa (for screw dislocation). The latter gives 125 MPa per at % Co, i.e. 55 MPa for 0.8 wt % Co. Considering the yield strength of Al–2.85 wt % Li–0.8 wt % Co following solution heat-treatment at 811 K for 0.5 h and ageing at 473 K for 16 h, the value in Table IV is seen to be 349 MPa. The estimated yield

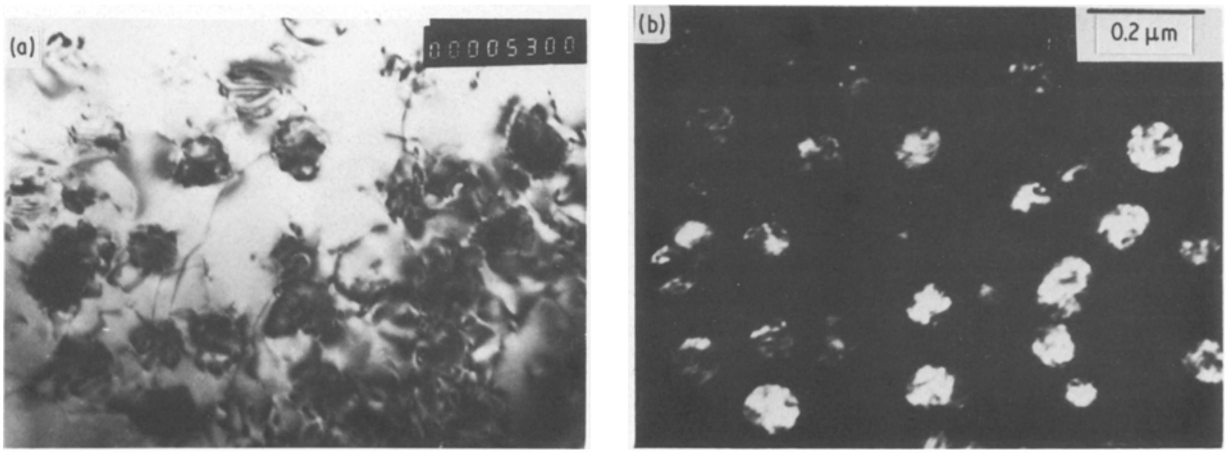

Figure 15 TEM micrographs of 10ALCR ribbons aged at 473 K for 100 h and pulled to failure: (a) bright field, (b) dark field imaged on a δ' reflection.

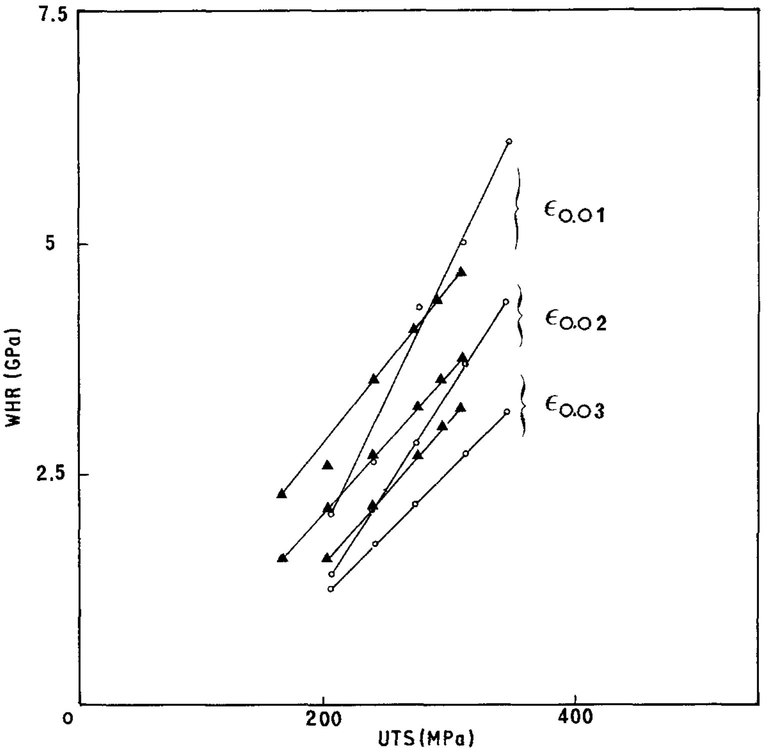

Figure 16 Variation of work-hardening rate (WHR) as a function of UTS for 10ALCR and 10ALCI alloys: (○) melt-spun, (▲) ingot metallurgy.

stress, taking the value of 76 MPa for the contribution of Al_9Co_2 dispersoids, is

$$\mathrm{YS(MPa)} = 43 + 220 + 76 = 339\,\mathrm{MPa} \quad (10)$$

whereas on taking the value of 55 MPa,

$$\mathrm{YS(MPa)} = 43 + 220 + 55 = 317\,\mathrm{MPa} \quad (11)$$

As can be seen the measured yield stress value is in good agreement with Equation 10.

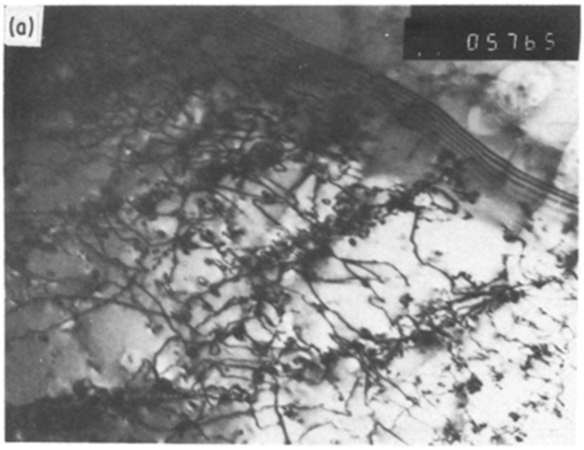

3.3. Fracture behaviour

Failure of 10ALCR in the peak-aged condition appears to be completely intergranular with significant grain (columnar) boundary separation below the fracture surface (Fig. 18). As can be seen, several sharp ledges are visible on the grain boundaries when the slip bands intersect the grain boundary. Addition of cobalt appears to change the mode of failure into transgranular through dimple formation. The dimples suggest a ductile type of fracture behaviour (Fig. 18b).

4. Summary and concluding remarks

1. The microstructure of melt-spun ribbons consists of elongated columnar grains (~30 to 40 μm). Their lengths represent the ribbon thickness whereas their diameters are about 1 to 3 μm.

2. Increasing the cobalt content increases the volume fraction of Al_9Co_2 phase particles. Their precipitation occurs in the matrix as well as at grain boundaries.

Figure 17 TEM micrographs of Al–Li–Co ribbons aged at 473 K for 16 h (peak-aged condition) and pulled to failure: (a) 40ALCR, (b) 80ALCR (bright field), (c) 80ALCR (dark field imaged on a δ' reflection).

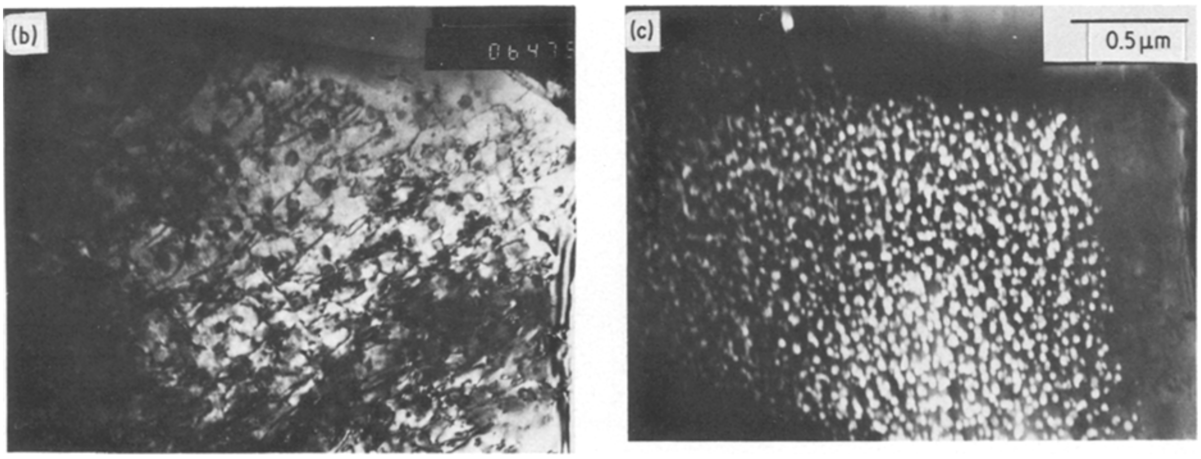

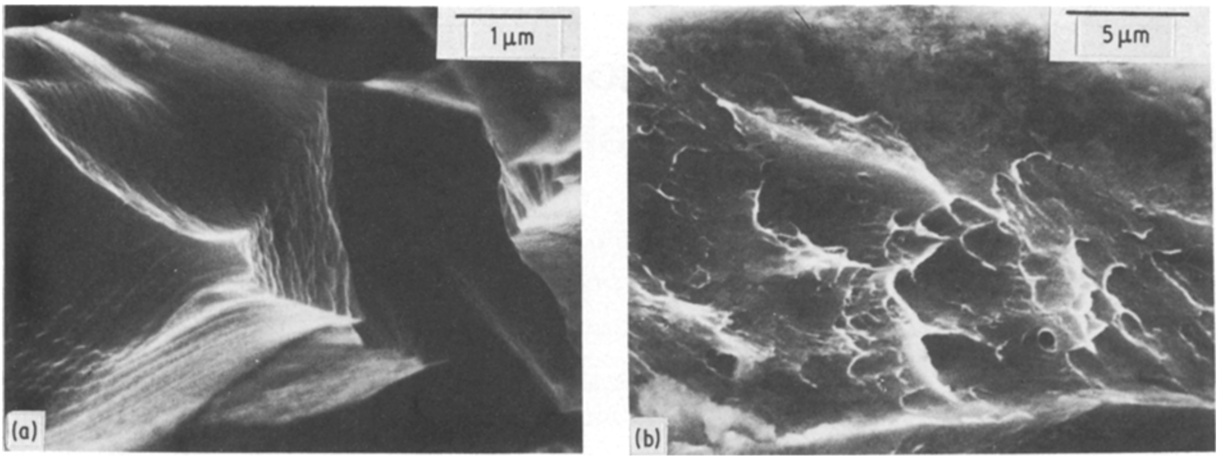

Figure 18 SEM micrographs of tensile fractures of Al–Li–Co ribbons aged at 473 K for 16 h: (a) 10ALCR, (b) 80ALCR.

Solution heat-treatment of 80ALCR results in eliminating the grain-boundary precipitation.

3. Suppression of the δ' (Al_3Li) phase particle nucleation reaction on melt-quenching is very difficult. The average coarsening rate is about $2.9 \times 10^{-25}\,m^3\,h^{-1}$. Coarsening of δ' particles as well as widening of precipitate-free zones follow a linear relation with $(\text{time})^{1/3}$.

4. Young's modulus (E) is determined for Al–2.85 wt % Li–0.1 wt % Co by two different methods, namely a bending test (for MS ribbons) and a tensile test (for IM alloy). In the peak-aged condition, the values of E are 80 to 83 and 80 to 82 GPa for MS and IM alloys, respectively. These values are confirmed by the Rule of Mixture equation

$$E_{\text{aged}} = E_{\text{m}} V_{\text{m}} + E_{\delta'} V_{\delta'}$$

5. Addition of cobalt continuously increases both the yield and ultimate tensile strengths, with a noticeable improvement in alloy ductility. The YS in the as-melt-spun condition is given by

$$\begin{aligned} \text{YS(MPa)} &= 22.15(\text{atomic fraction Li})^{1/2} \\ &\quad + 125(\text{atomic fraction Co}) \end{aligned}$$

However, after ageing, the YS is simply given by a summation of the contributions of lithium in solid solution, δ' precipitation and that of the Al_9Co_2 dispersoids.

6. In the peak-aged condition, deformation of Al–2.85 wt % Li–0.1 wt % Co is attributed to the formation of localized slip bands that develop following precipitate shearing. Increasing cobalt up to 0.8 wt % and, in turn, the volume fraction of Al_9Co_2 dispersoids is sufficient to disperse the slip bands and to promote homogeneous deformation. Fracture of the former alloy appears to occur mainly by the low-energy intergranular mode, whereas the high-energy transgranular mode is the main mechanism for the latter.

Acknowledgements

The author wishes to thank Professor G. Champier, Director, Laboratoire de Physique du Solide, Ecole des Mines, for suggesting the problem and for his constant encouragement and fruitful discussions. Thanks are also extended to Dr C. Téte and Mr J. Rohr in particular, as well as to members of the laboratory for their help and assistance.

References

1. T. H. SANDERS Jr and E. S. BOLMUTH, *Met. Prog.* **113** (1978) 32.
2. D. WEBSTER, *Met. Trans.* **10A** (1978) 1913.
3. T. H. SANDERS Jr and E. A. STARKE Jr, *Acta Metall.* **30** (1982) 927.
4. R. K. GARRETT Jr and T. H. SANDERS Jr, *Mater. Sci. Eng.* **60** (1983) 269.
5. P. N. T. UNWIN and R. B. NICHOLSON, *Acta Metall.* **17** (1969) 1379.
6. E. P. BUTLER and P. R. SWANN, *ibid.* **24** (1976) 343.
7. S. LARTIQUE and L. PRIESTER, *ibid.* **31** (1983) 1809.
8. N. J. GRANT, *J. Metals* **35** (1983) 20.
9. B. NOBLE and G. E. THOMPSON, *Metal Sci.* **5** (1971) 114.
10. L. N. TROFIMOVA and K. V. CHINOTOV, *Phys. Met. Metall.* **44** (1978) 94.
11. S. CERESARA, G. COCCA, G. FRAGHROZZI and L. SCHIFFINIC, *Phil. Mag.* **35** (1977) 37.
12. T. H. SANDERS Jr, E. A. LUDWVEZAKE and R. P. SAWTELL, *Mater. Sci. Eng.* **43** (1980) 247.
13. D. B. WILLIAMS and J. W. EDINGTON, *Met. Sci.* **9** (1975) 519.
14. G. W. LORIMER and R. B. NICHOLSON, *Acta Metall.* **14** (1966) 1009.
15. M. HANSEN, "Constitution of Binary Alloys", 2nd Edn (McGraw-Hill, London, 1958) p. 79.
16. B. NOBLE, S. J. HARRIS and K. DINSDALE, *J. Mater. Sci.* **17** (1982) 461.
17. A. GYSLER, R. CROOKS and E. A. STARKE Jr, in Proceedings of 7th Conference on Light Metals, Loeben-Vienna, 1981.
18. S. J. HARRIS, private communication (1980).
19. N. J. GRANT, S. KING and W. WANG, "Aluminium-Lithium Alloys" (The Metallurgical Society of AIME, Warrendale, Pennsylvania, 1981) p. 171.
20. H. GLEITER and E. HORNBOGEN, *Mater. Sci. Eng.* **2** (1967/68) 285.
21. M. F. ASHBY, *Phil. Mag.* **21** (1970) 335.
22. H. TAMLER and O. KANERT, *Acta Metall.* **32** (1984) 1205.
23. K. K. SANKARAN, J. E. O'NEAL and S. M. L. SASTRY, *Metall. Trans.* **14A** (1983) 2174.

Received 12 June
and accepted 23 October 1985